Two-Port, Dual-Circularly Polarized, Low-Profile Broadside-Radiating Electrically Small Huygens Dipole Antenna

Zhentian Wu, Ming-Chun Tang, Ting Shi, and Richard W. Ziolkowski

***Abstract*—A two-port dual-circularly polarized (CP), low-profile broadside-radiating electrically small Huygens dipole antenna is presented that has an advanced feed network and multilayer stacked layout of its electric and magnetic near-field resonant parasitic (NFRP) elements. It radiates left-hand CP (LHCP) or right-hand CP (RHCP) fields at its 1.5 GHz resonance frequency depending on the selected feed port. The measured results, in good agreement with the simulated values, demonstrate that the antenna is electrically small (*ka* = 0.94) and low-profile (0.053 λ_0), relative to the longest wavelength in its -10-dB impedance bandwidth. The port isolation is over 15.6 dB within its 0.99% fractional impedance bandwidth. When port 1 (port 2) is excited, its measured peak realized gain and front-to-back ratio (FTBR) values are, respectively, 1.82 dBi (1.81 dBi) and 4.1 dB (4.5 dB).**

***Index Terms*—Dual-circular polarization, electrically small antennas, Huygens dipole antennas, near-field resonant parasitic (NFRP) elements**

I. Introduction

Electrically small Huygens dipole antennas have received increased attention in recent years due to their advantageous radiation performance characteristics for a variety of wireless systems. For example, they can exhibit high directivities, large front-to-back ratios (FTBR) and wide beamwidths without the requirement of additional constructs such as slot structures [1], periodic electromagnetic band gap structures (EBG) [2], or reflector elements [3]. A variety of Huygens dipole electrically small antennas (ESAs) have been reported with different polarization features, i.e., linearly polarized (LP) [4]-[5] and circularly polarized (CP) [6-7] designs. Among them, the CP Huygens dipole ESAs have advantages over the LP ones in applications to radio-frequency identification devices (RFIDs) and radar tracking systems since they reduce multipath interference and allow for flexible alignments of the transmitter and receiver antennas [8]. Nonetheless, a single antenna that produces dual states of polarization [9-10] would be very useful. It would reduce the total number of units in a system, increase the link capacity, and realize frequency reuse. Even though the dual-LP Huygens dipole ESA was accomplished in [11], polarization mismatch problems for certain wireless applications, e.g., RFIDs and radar tracking systems, would arise due to the possible misalignment of the transmitting and receiving antennas [8]. Therefore, a Huygens dipole ESA that radiates both right- and left-hand circular polarization (RHCP and LHCP) would be a very attractive practical development.

The realization of dual-CP performance in an electrically small, low profile system is challenging. In particular, one must achieve high isolation between its two closely-placed ports, one for each polarization state. High isolation in dual-CP designs has been reported using different technologies. These include hybrid couplers [9-10], [12], even-odd mode feed networks [13], loading modified slot feeding structure below a metasurface [14], strategic placements of inverted L-shaped grounded strips [15], and decoupling networks [16]. However, they all require very large ground planes [9-10], [12-15] or long feedlines [16]. These aspects make their total electrical size inescapably large, e.g., $ka > 2.13$ [9], where $k = 2\pi/\lambda_0$ and a is the radius of the smallest sphere that completely encloses the entire antenna system at the operational free-space wavelength λ_0. To the best of our knowledge, there have been few dual-CP ESA designs ($ka < 1$) reported to the date, let alone broadside radiating ones.

In this Communication, an electrically small, low-profile, Huygens dipole antenna with dual-CP radiation performance characteristics is reported. Different from the methods discussed previously, an advanced approach is introduced to successfully achieve the dual-CP Huygens dipole ESA. It consists of a stacked set of capacitively loaded loop (CLL) and Egyptian axe dipole (EAD) near-field resonant parasitic (NFRP) elements. A compact, balanced feed network specifically tailored to accommodate these NFRP elements and their exciting dipoles is developed. Its optimized architecture leads to a large isolation between its two ports. The antenna configuration is introduced in Section II, and its design parameters are detailed. A prototype of this antenna was fabricated and measured; details are presented in Section III. The measured results are shown to be in agreement with the simulated values. They demonstrate that the prototype is electrically small, low-profile, and exhibits high port isolation within its -10-dB impedance bandwidth. To understand the design principles more completely, the physical mechanisms that lead to its dual-CP radiation performance and high port isolation are detailed. Finally, some conclusions are drawn in Section IV. All of the numerical simulations and their optimizations reported herein were performed using the commercial software ANSYS/Ansoft HFSS, version 18. The simulation models employed the known, real properties of the dielectrics and conductors.

II. Dual-CP Huygens Dipole ESA Design

The geometric structure of the dual-CP Huygens dipole ESA is shown in Fig. 1 and the corresponding optimized design parameters are given in Table I. As illustrated in Figs. 1(a) and (b), the proposed dual-CP ESA consists of eight substrate layers which all have the same radius: R1 = 30.0 mm. Layer_1 is a Rogers 4350B copper-cladded substrate (relative dielectric constant ε_r = 3.48, loss tangent tan δ = 0.0037, and substrate height h1 = 0.254 mm). Layer_2 - Layer_4 are each a Rogers 5880 copper-cladded substrate (ε_r = 2.2, tan δ = 0.0009, and substrate height h2 = h3 = h4 = 0.254 mm). The

Manuscript received on 12th, December, 2019; revised on 22nd, May, 2020; and accepted on 26th, May, 2020…

This work was supported in part by the National Natural Science Foundation of China contract number 61922018; in part by the Graduate Scientific Research and Innovation Foundation of Chongqing, China contract number CYS18062; in part by the Funding of the leading research talent cultivation plan of Chongqing University contract number cqu2017hbrc1A08; in part by the Chongqing Natural Science Foundation contract number cstc2019jcyjjqX0004; and in part by the Australian Research Council grant number DP160102219. *(Corresponding author: Ming-Chun Tang.)*

Z. Wu, M.-C. Tang, and T. Shi are with the Key Laboratory of Dependable Service Computing in Cyber Physical Society Ministry of Education, School of Microelectronics and Communication Engineering, Chongqing University, Chongqing 400044, China (E-mail: tangmingchun@cqu.edu.cn).

R. W. Ziolkowski is with the University of Technology Sydney, Global Big Data Technologies Centre, Ultimo NSW 2007, Australia (E-mail: Richard.Ziolkowski@uts. edu.au).

remaining four layers are each a Rogers 4350B laminate substrate (substrate height h5 = h7 = 0.254 mm, h6 = 1.524 mm, h8 = 0.10 mm).

For ease of description, the magnetic elements 1 and 2 and the electric elements 1 and 2 are labeled as M1, M2, E1, and E2, respectively. The upper and lower surfaces of the substrate layers constituting M1, E1, M2, E2, and the driven elements are shown in Figs. 1 (c)−(g). The copper patches of M1 lie on the upper surface of both Layer_1 and Layer_5. They are connected by four metal cylindrical posts, which pass through Layer_1 to Layer_4. Each has the height h12 = 8.5 mm and a 1.25 mm radius. The element E1 is placed on the lower surface of Layer_3. The related excitation copper strips are placed on the upper surface of Layer_6 and lower surface of Layer_8, and are connected to Port 1. Two vias, each with a 0.2 mm radius, pass from Layer_6 to Layer_8 to connect these copper strips. Similarly, the copper patches of M2 lie on the upper surface of Layer_2 and the lower surface of Layer_6, respectively. There are four circular copper pads (each has a 2.95 mm radius) located on the upper surface of Layer_5, which connected the copper patches lie on the upper surface of Layer_2 by four metal cylindrical posts (each has the height h11 = 7.3 mm and a 1.25 mm radius). Four vias, each with a 1.25 mm radius, pass from Layer_5 to Layer_6 to connect the copper patches that lie on the lower surface of Layer_6 and the four circular copper pads. The element E2 lies on the upper surface of Layer_4. The related excitation copper strips lie on the upper and lower surfaces of Layer_8 and are connected with port 2. Two vias, each with a 0.2 mm radius, connect them.

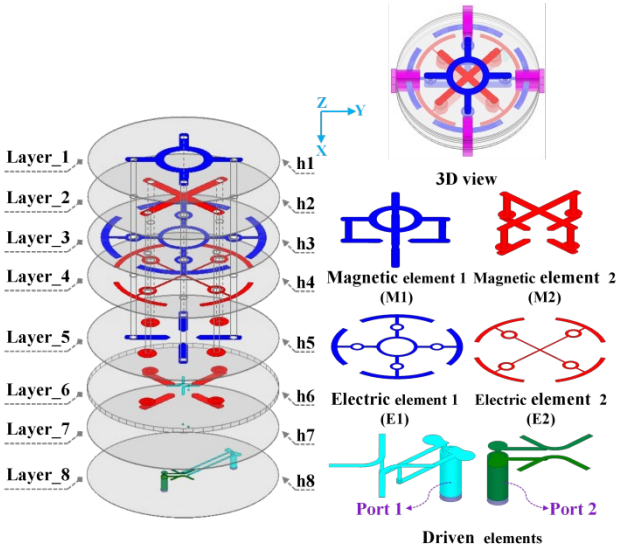

(a)

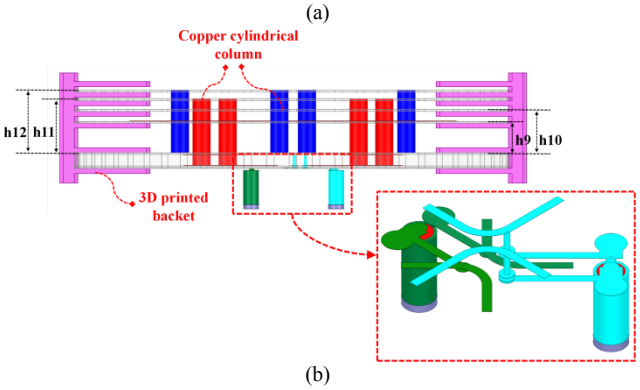

(b)

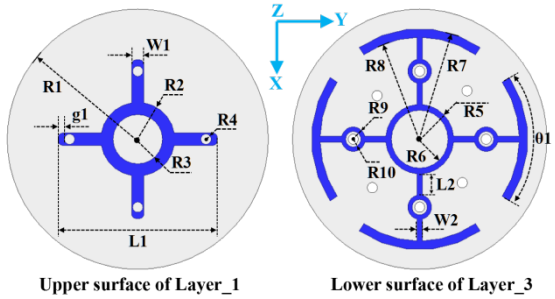

(c)

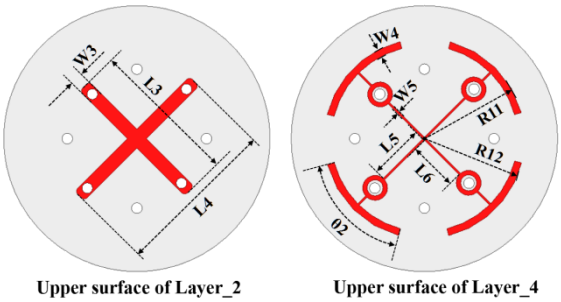

(d)

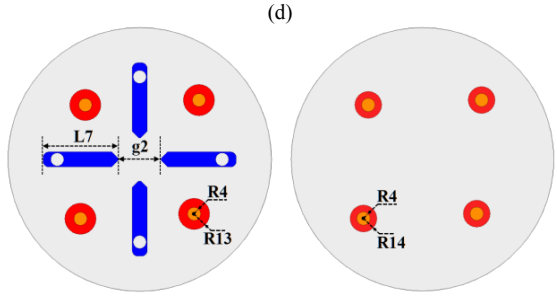

(e)

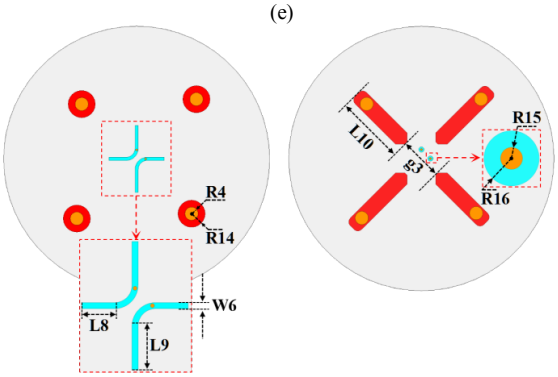

(f)

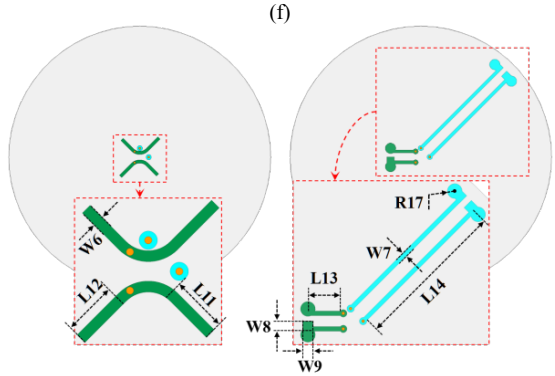

(g)

Fig. 1 Geometry of the dual-CP Huygens dipole ESA. (a) 3-D isometric view. (b) Side view. (c) Upper surface of Layer_1 and Lower surface of Layer_3. (d) Upper surface of Layer_2 and Layer_4. Upper and lower surfaces of (e) Layer_5, (f) Layer_6, (g) Layer_8.

TABLE I. THE OPTIMIZED DUAL-CP HUYGENS DIPOLE ESA PARAMETERS (IN MM)

h1=0.254	*h6=1.524*	*h8=0.1*	*h9=4.28*	*h10=5.92*
h11=7.3	*h12=8.5*	*L1=36.6*	*L2=4.87*	*L3=34.3*
L4=36.9	*L5=12.71*	*L6=11.41*	*L7=14.2*	*L8=3.2*
L9=4.3	*L10=14.3*	*L11=2.8*	*L12=3.2*	*L13=4.75*
L14=21.42	*W1=2.8*	*W2=1.4*	*W3=3*	*W4=1.6*
W5=0.6	*W6=0.6*	*W7=0.6*	*W8=1.25*	*W9=1.4*
R1=30	*R2=9.1*	*R3=6.3*	*R4=1.25*	*R5=8.1*
R6=6.7	*R7=25.9*	*R8=23.5*	*R9=2.8*	*R10=1.8*
R11=22.6	*R12=22.55*	*R13=2.95*	*R14=2.55*	*R15=0.2*
R16=0.5	*R17=0.5*	*g1=1.4*	*g2=8.2*	*g3=8.3*
θ1=70°	*θ2=62°*	*Null*		

According to the design principles reported in [17], a CP ESA is achieved by feeding two orthogonally oriented LP ESAs with a π/2 phase shift. The segments of the orthogonal M1 and E1 elements that are located along the *x*- and *y*-axes are excited simultaneously by the driven element connected to port 1. They form the LHCP Huygens dipole ESA. Similarly, the RHCP Huygens dipole ESA is achieved with the orthogonal M2 and E2 elements, which are oriented ± 45° with respect to the *x*- and *y*-axes. They are excited by the driven element connected to port 2.

Several design details must be elucidated. All of the NFRP elements are 90° rotationally symmetric. Thus, the requisite π/2 phase shifts are obtained by introducing asymmetries. The LHCP operation is achieved with the currents induced on M1 and E1 by the asymmetrical feedline driven by port 1, which lies on the upper surface of Layer_6. It is asymmetric because L8 is not equal to L9. On the other hand, the π/2 phase shift for the RHCP operation is generated by the asymmetry of both M2 and E2 along the ± 45° directions, i.e., their total lengths are not the same along the +45° and -45° directions (i.e., L3 ≠ L4 and R11 ≠ R12). Furthermore, good impedance matching to the 50-Ω sources, port 1 and port 2, was obtained without any external matching network. By simply adjusting the asymmetric lengths of the feedlines from two ports, i.e., L8 ≠ L9 and L11 ≠ L12, the capacitive coupling between the associated NFRP and driven elements was regulated and the impedance matching subsequently optimized.

Note that in contrast to M2 and E2, both M1 and E1 have an additional copper ring in their design (with inner radius R3 and outer radius R2 for M1, and with inner radius R6 and outer radius R5 for E1) located at the centers of their substrates. The additional copper ring on M1 and E1 reduces the overlapping area between M2 and E2 along the +*z*-axis. This arrangement facilitates the improved radiation efficiencies of the both radiators. Moreover, the copper strips of M1and M2 and E1 and E2 are approximately orthogonal to each other in the overlapping ring area. This arrangement enhances the isolation between M1 and M2, and between E1 and E2.

Also note that our initial simulation studies identified that if either M1 or M2, or the feedlines from either of the two ports were placed on the upper and lower surfaces of the same substrates, the isolation between the two ports was quite poor, i.e., lower than 10 dB. Consequently, the lower face of M1 was placed on the upper surface of Layer_5 and the lower face of M2 was placed on the lower surface of Layer_6 in the final design in order to improve the isolation between the two ports. Concomitantly, the feedlines of port 1 and port 2 were placed on the upper surfaces of Layer_6 and Layer_8 to excite the M1-E1 (LHCP element) and M2-E2 (RHCP element) pairs, respectively. To maintain the relative vertical distance between these layers, four 3D printed brackets were employed. Our simulation studies indicated that the 3D printed brackets only have a very small impact on the antenna performance.

III. SIMULATED AND MEASURED RESULTS

A. Results and Performance

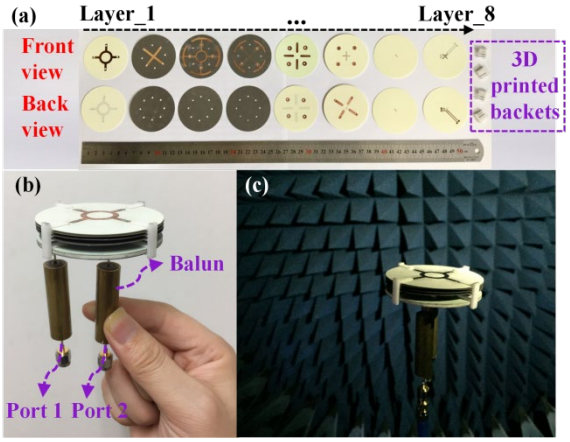

Fig. 2 Fabricated prototype of the dual-CP Huygens dipole ESA. (a) Front and back views of each layer before assembly. (b) Side view of the assembled antenna mounted on two sleeve baluns, one for each port. (c) 3-D isometric view of the AUT in the anechoic measurement chamber.

The dual-CP Huygens dipole ESA in Fig. 1 was fabricated, assembled, and measured. Photographs of all of its component parts before assembly are presented in Fig. 2(a). The assembled dual-CP Huygens dipole ESA was mounted on two sleeve baluns, one for each port, as shown in Fig. 2(b). Because the balanced driven elements were directly connected to the unbalanced 50-Ω coaxial cables, two 43 mm-long sleeve baluns (~$0.21\lambda_0$) were employed to mitigate any spurious currents induced on the outer wall of the long coax cables and ensured the accuracy of the measurements of the S-parameters and the far-filed directivity pattern characteristics [18]. The S-parameters of the dual-CP ESA were measured with an Agilent E8361A PNA vector network analyzer (VNA). Its far-field radiation performance characteristics were measured in an anechoic chamber at University of Electronic Science and Technology of China, Chengdu, China, which utilizes an Agilent N5230A PNA-L VNA and a SATIMO passive measurement system. The antenna under test (AUT) in this chamber is shown in Fig. 2(c).

The measured and simulated performance characteristics of the dual-CP Huygens dipole ESA (taking into account of the balun presence) are presented in Figs. 3-4. As shown in Fig. 3, the measured (simulated) overlapped –10-dB impedance bandwidth ($|S_{11}| \leq$ -10 dB) for both ports was 14 MHz, covering 1.495 to 1.509 GHz (16 MHz, covering 1.501 to 1.517 GHz) and the corresponding fractional impedance bandwidth (FBW) was 0.99% (1.12%). The measured (simulated) isolation between the two ports was greater than 15.6 (16) dB, which is higher than the standard requirement of 15 dB for dual-CP antennas [9]. The measured (simulated) axial ratio (AR) values are also plotted in Fig. 3. The overlapped 3-dB AR bandwidth reaches 14 MHz, from 1.495 to 1.509 GHz (15 MHz, from 1.502 to 1.517 GHz). For the CP antennas, the usable bandwidth contains the –10-dB impedance bandwidth and the 3-dB AR bandwidth. Thus, the entire measured AR passband was usable. The corresponding measured (simulated) overall electrical size and height of the system at the center of the operational frequency range $f_{0,\,meas}$ = 1.502 GHz ($f_{0,\,sim}$ = 1.509 GHz) were *ka* = 0.94 (0.948) and $0.047\lambda_0$ ($0.048\lambda_0$), respectively.

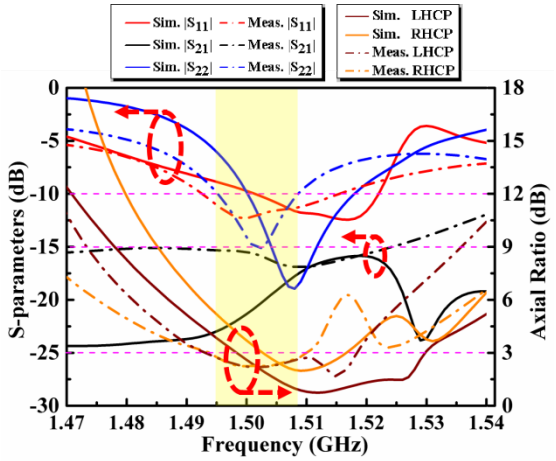

Fig. 3 Measured and simulated S-parameters and AR values of the dual-CP Huygens dipole ESA.

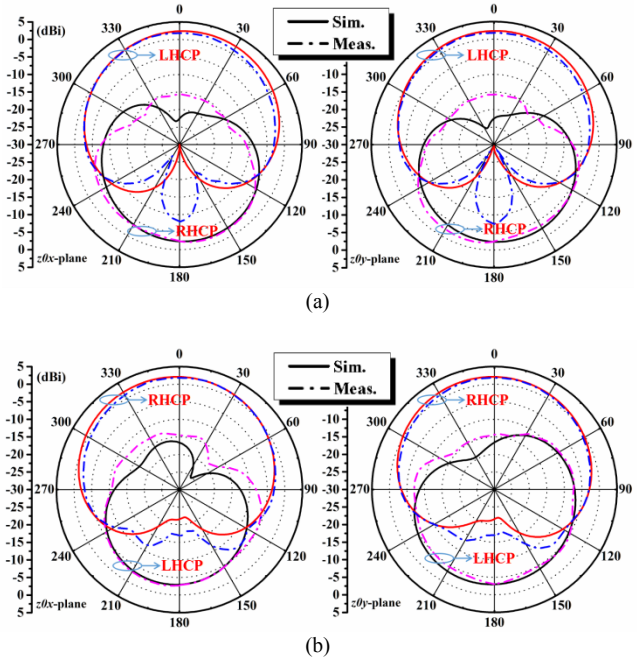

(a)

(b)

Fig. 4 Measured (simulated) 2-D RG patterns of the dual-CP Huygens dipole ESA. (a) LHCP is dominant at 1.50 (1.508) GHz when port 1 is excited. (b) RHCP is dominant at 1.502 (1.509) GHz when port 2 is excited.

The measured and simulated realized gain (RG) patterns in the *z0x*- and *z0y*- planes are given in Fig. 4. When port 1 was excited, LHCP fields were radiated with their maximum in the +*z* direction. The measured (simulated) peak RG value, 1.82 (2.36) dBi, was reached at 1.50 (1.508) GHz with a FTBR = 4.1 (4.7) dB and a radiation efficiency (RE) = 71.8% (84.3%). The measured (simulated) half-beam coverage was 134°, from -68° to 66° (136°, from -60° to 76°) in the *z0x*-plane and 132°, from -68° to 64° (139°, from -65° to 74°) in the *z0y*-plane. Similarly, when port 2 was excited, RHCP fields were radiated maximally in the +*z* direction. The measured (simulated) peak RG value was 1.81 (2.06) dBi at 1.502 (1.509) GHz with a FTBR = 4.5 (4.9) dB and RE = 72.6% (75%). The measured (simulated) half-beam coverage was 134°, from -66° to 68° (144°, from -81° to 63°) in the *z0x*-plane and 135°, from -67° to 68° (143°, from -73° to 70°) in the *z0y*-plane.

In addition, compared with the simulated S-parameters values, the measured ones were slightly red-shifted to lower frequencies, as observed in Fig. 3. The main reasons for this phenomenon are ascribed to the small dimensional errors generated during the fabrication and assembly stages. For example, the height of the eight fabricated metal columns was not quite the same as the simulated values (h11 and h12) after the structure was assembled, which impacted the relative distances between and the parallel orientation of the substrate layers. According to our simulation studies, the higher relative distances would lower the operational frequency range.

B. Operating Mechanisms

In order to explain its operational mechanisms, the case when port 1 is excited is demonstrated as an illustrative example. The current distributions on the main metallic surfaces of the dual-CP Huygens dipole ESA are presented and analyzed at the resonance frequency 1.509 GHz, as is shown in Fig. 5. The current distributions on the feedlines and upper surfaces of M1 and E1 at the times 0, T/4, T/2, and 3T/4, where T is one source period, are highlighted in Fig. 5. The additional solid purple (referring to the feedlines), blue (referring to the upper face of M1), and orange (referring to the E1) arrows annotate their directional behavior.

As is known [17], the CP radiation can be obtained with NFRP antennas by exciting their orthogonal LP NFRP elements with equal amplitude and a $\pi/2$ phase difference. Elements M1 and E1 could form such a pair of two orthogonal LP Huygens dipole radiators. Their orientations are along the *x*- and *y*-axis, respectively. As explained, the requisite $\pi/2$ phase difference is produced by the asymmetric feedline connected to port 1. Taking the blue arrows as an example, their current vector direction along the *y*- and *x*- axes rotates in the clockwise direction, shown in Fig. 5 (a). The LHCP field is thus generated and has its maximum along the +*z* direction.

In order to illustrate the mechanism producing the high isolation between the two ports, the current distributions on the feedlines and upper surfaces of M2 and E2 when port 1 is excited are presented in Fig. 5 (b). These surface currents are annotated with the additional red solid arrows to clarify their directional behaviors. The red arrows are usually opposite along both the ± 45° directions. As a result, these opposite currents cancel each other out and yield a nearly complete offset of their impact on port 1. However, it is observed that a small portion of the surface currents on E2 are still oriented along the same direction near the times 0, T/4, T/2, and 3T/4. Thus, they have a small impact on the port isolation. This is the reason why the isolation in this dual-CP is only design 16 dB, which is not as high as it was in the dual-LP ESA (25.8 dB) reported in [11]. Nonetheless, it is still quite a good value and better than the standard 15 dB criterion. When port 2 is excited, the asymmetric M2 and E2 elements generate the requisite $\pi/2$ phase shift, and their equivalent vectors in the ± 45° directions rotate in the counter-clockwise direction, yielding the RHCP fields.

C. Parameter studies

Guidelines for the design of a one-port Huygens dipole ESA have been detailed in [5]. In this dual-CP design, the magnetic dipole is also more strongly coupled to the driven element than the electric dipole does. This occurs because the magnetic dipole is closer to the driven element than the electric dipole. Consequently, the overall size of magnetic dipole plays an important role in determining the Huygens ESA's operational frequency. On the other hand, the electric dipole is placed near to the center of the magnetic dipole. This close proximity of the electric and magnetic dipoles leads to a strong mutual coupling, which in turn leads to the currents being driven on the electric dipole.

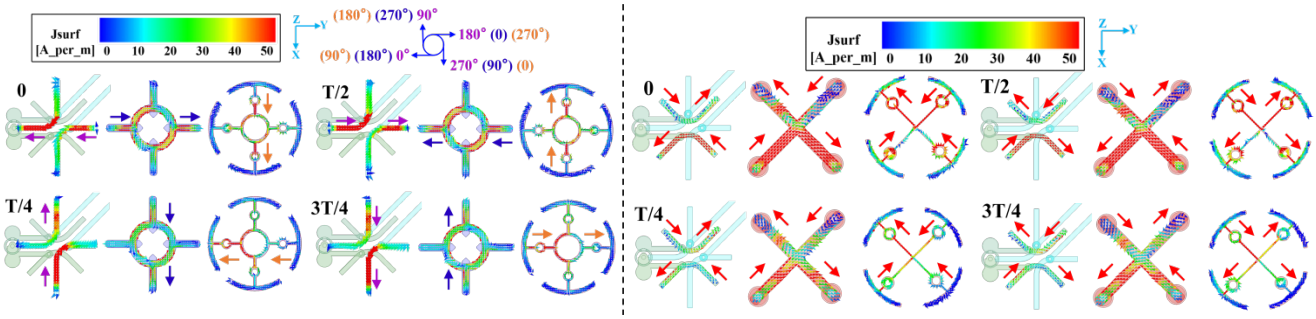

Fig.5 Surface current distributions on the driven and NFRP elements for the dual-CP Huygens dipole ESA operating in its LHCP mode, i.e., with port 1 active. (a) Elements M1 and E1 are associated with port 1. (b) Elements M2 and E2 are associated with port 2.

TABLE II
COMPARISON OF THE DUAL-CP HUYGENS DIPOLE ANTENNA WITH RELATED DUAL-CP ANTENNAS REPORTED IN THE LITERATURE

Ref.	ka	FBW (%)	RG (dBi)	FTBR (dB)	Isolation (dB)	Electrical Size (λ_0^3)	Beam Direction	Ground Dependent
[9]	2.12	4	6	30	> 15	0.5 × 0.5 × 0.057 = 0.0143	Broadside	yes
[12]	7.03	3	5.3	18	> 14	1.9 × 1.16 × 0.02 = 0.0441	Endfire	yes
[13]	3.15	1.3	4.8	-	> 10	0.73 × 0.69 × 0.02 = 0.0101	Endfire	yes
[14]	3.17	31.3	7.01	18	> 10	0.71 × 0.71 × 0.04 = 0.0202	Broadside	yes
[15]	2.66	60	-	-	> 15	0.6 × 0.6 × 0.016 = 0.0058	Broadside	yes
This work	0.94	0.99	1.81	4.1	> 15.6	$\pi \times (0.15)^2 \times 0.053 = 0.0037$	Broadside	no

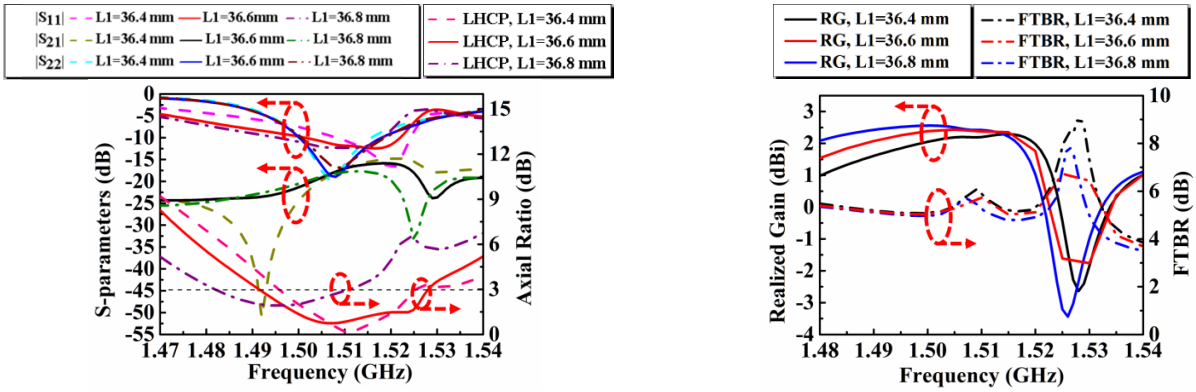

Fig. 6 The effect of the M1 length L1 on the performance characteristics of the dual-CP Huygens dipole ESA. (a) The S-parameters and AR values. (b) The RG and FTBR values.

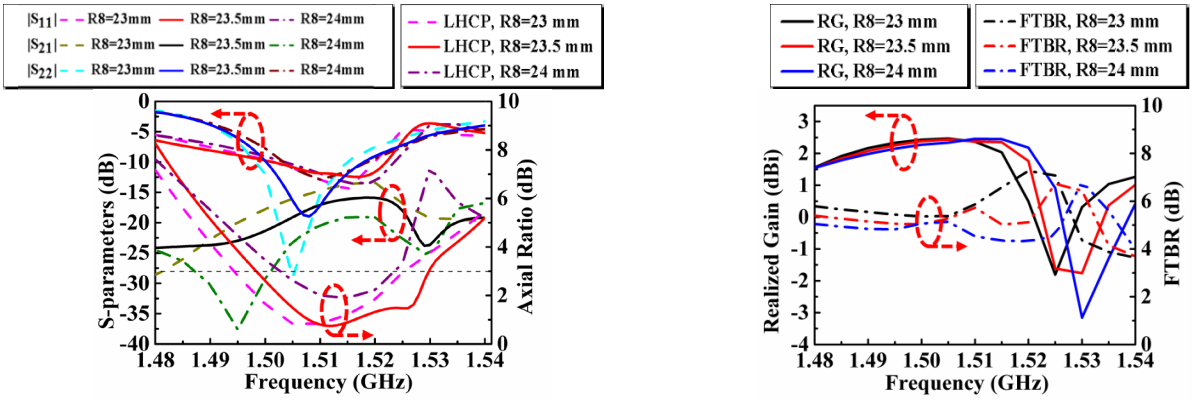

Fig. 7 The effect of the E1 length R8 on the performance characteristics of the dual-CP Huygens dipole ESA. (a) The S-parameters and AR values. (b) The RG and FTBR values.

Therefore, the Huygens dipole antenna's operational performance characteristics (including its $|S_{11}|$, RG, FTBR, etc.) can be optimized by changing the electric dipole's dimensions and the distance between it and the magnetic dipole. Furthermore, we carried out numerical studies on the several important design parameters that guide the design and optimization of our reported dual-CP Huygens dipole ESA. The results were obtained by varying one constructive parameter while keeping all others fixed. First, Fig. 6 presents the effect of the lengths of the M1 (L1) on the S-parameters, AR, RG and FTBR values, respectively. The change of L1 greatly influences the operating frequency. This confirms that the magnetic dipole size plays an important role in determining it. Similarly, the 3-dB AR bandwidths witness corresponding changes. As L1 increases, the RG values will increase, but it has little impact on the FTBR values. Second, when the

length of the E1 (R8) changes, the radiation performance characteristics and the isolation are significantly influenced, but the operational bandwidth is essentially unchanged as Fig. 7 shows. Third, by adjusting the asymmetry lengths (i.e., L8 and L9) of the feedline of port 1 and the size of M2 and E2 (i.e., L3, L4 for M2 and R11, R12 for E2), the AR values of LHCP and RHCP states can be effectively optimized. As an example, Fig. 8 presents the effect of changing the length of the port 1 feedline, L9, on the S-parameters and AR values. It is clear that the variation of L9 affects the $|S_{11}|$ values and the isolation level between the ports, as well as the AR values of the LHCP state.

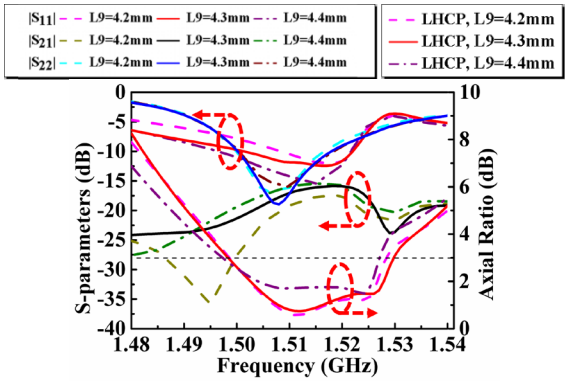

Fig. 8 The effect of the port 1 feedline length L9 on the S-parameters and AR values of the dual-CP Huygens dipole ESA.

To understand the efficacy of our developed dual-CP design, fair comparisons of its prototype's performance and several recently reported dual-CP antennas are given in Table II. The listed performance characteristics are comprehensive. They include the electrical sizes, FBWs, RG values, FTBR values, isolation levels, main beam directions and ground-dependent features. Table II highlights the fact that this dual-CP Huygens dipole antenna achieves very good port isolation without a ground plane. It also demonstrates that it is electrically small and low-profile, and emits broadside directed fields. Concurrently, the table also indicates that it has, as anticipated, a reasonably narrow bandwidth because of its electrically small size. Nevertheless, an enhancement of its bandwidth could be realized by introducing non-Foster elements as has been experimentally accomplished in [19]. To further emphasize the very good port isolation achieved with our electrically small system, we have performed simulation studies of the other designs, which are all electrically large. We have determined that their reported high-level port isolation values, for example, the cavity-backed design in [9], significantly deteriorate as their *ka* values approach 1.0.

IV. Conclusion

A dual-CP, low-profile, broadside-radiating, electrically small Huygens dipole antenna was demonstrated. It radiated LHCP or RHCP fields depending on the selected feed port and exhibited high isolation between its two ports. The requisite $\pi/2$ phase shift to realize the LHCP or RHCP radiation performance was accomplished by asymmetric sizes of its driven and NFRP elements. The LHCP and RHCP element pairs are oriented 45° with respect to each other. Their asymmetric lengths were tuned to achieve capacitive and inductive behaviors that naturally lead to the required $\pi/2$ phase shifts. The entire system consisted of eight substrate layers to accommodate all of the components of the driven and NFRP elements. The layered structure aided achieving large port isolation despite the presence of the many small copper elements in the design.

The electrically small size of the two-port dual-CP Huygens dipole prototype, its high two-port isolation and its wide beamwidth patterns empower it as an excellent candidate for a variety of narrowband wireless applications requiring high performance and multifunctional compact radiating and receiving elements, e.g., GPS and RFID systems associated with future 5G (fifth generation) and IoT (internet-of-things) ecosystems. Future efforts include improving the broadside-radiating performance of the reported dual-CP Huygens dipole ESA while maintaining its exceptional port isolation.

References

[1] M.-C. Tang and R. W. Ziolkowski, "Efficient, high directivity, large front-to-back-ratio, electrically small, near-field-resonant-parasitic antenna," *IEEE Access*, vol. 1, no. 1, pp. 16 - 28, May 2013.

[2] J. Ng and R. W. Ziolkowski, "Combining metamaterial-inspired electrically small antennas with electromagnetic band gap (EBG) structures to achieve higher directivities and bandwidths," in *Proc. 2012 International Workshop on Antenna Technology (iWAT 2012)*, Tucson, America, pp. 189-192, Mar. 2012.

[3] S. Lim and H. Ling, "Design of electrically small Yagi antenna," *Electron. Lett.*, vol. 43, no. 5, pp. 3–4, Mar. 2007.

[4] R. W. Ziolkowski, "Low profile, broadside radiating, electrically small Huygens source antennas," *IEEE Access*, vol. 3, pp. 2644–2651, 2015.

[5] M.-C. Tang, H. Wang, and R. W. Ziolkowski, "Design and testing of simple, electrically small, low-profile, Huygens source antennas with broadside radiation performance," *IEEE Trans. Antennas Propag.*, vol.64, no. 11, pp. 4607-4617, Nov. 2016.

[6] P. Alitalo, A. O. Karilainen, T. Niemi, C. R. Simovski, and S. A.Tretyakov, "Design and realisation of an electrically small Huygens source for circular polarization," *IET Microw. Antennas Propag.*, vol. 5, no. 7, pp. 783-789, 2011.

[7] W. Lin and R. W. Ziolkowski, "Electrically small, low-profile, Huygens circularly polarized antenna," *IEEE Trans. Antennas Propag.*, vol. 66, no. 2, pp. 636-643, Feb. 2018.

[8] S. Gao, Q. Luo, and F. Zhu, *Circularly Polarized Antennas. Hoboken*, NJ, USA: Wiley, Nov. 2013.

[9] R. Ferreira, J. Joubert, and J. W. Odendaal, "A compact dual-circularly polarized cavity-backed ring-slot antenna," *IEEE Trans. Antennas Propag.*, vol. 65, no. 1, pp. 364-368, Jan. 2017.

[10] Y.-H. Yang, B.-H. Sun, and J.-L. Guo, "A low-cost, single-layer, dual circularly polarized antenna for millimeter-wave applications," *IEEE Antennas Wirel. Propag. Lett.,* vol. 18, pp. 651-655, 2019.

[11] M.-C. Tang, Z. Wu, T. Shi, H. Zeng, W. Lin, and R. W. Ziolkowski, "Dual-linearly-polarized, electrically small, low-profile, broadside radiating, Huygens dipole antenna," *IEEE Trans. Antennas Propag.*, vol. 66, no. 8, pp. 3877-3885, Aug. 2018.

[12] A. Wang, L. Yang, Y. Zhang, X. Li, X. Yi, and G. Wei, "A novel planar dual circularly polarized endfire antenna," *IEEE Access*, vol. 7, pp. 64297–64302, 2019.

[13] A. Narbudowicz, X. Bao, and M. J. Ammann, "Dual circularly-polarized patch antenna using even and odd feed-line modes," *IEEE Trans. Antennas Propag.*, vol. 61, no. 9, pp. 4828-4831, Sep. 2013.

[14] S. Liu, D. Yang, and J. Pan, "A low-profile broadband dual-circularly-polarized metasurface antenna," *IEEE Antennas Wirel. Propag. Lett.,* vol. 18, pp. 1395-1399, 2019.

[15] R. K. Saini and S. Dwari, "A broadband dual circularly polarized square slot antenna," *IEEE Trans. Antennas Propag.*, vol. 64, no. 1, pp. 290-294, Jan. 2016.

[16] L. Lu, Y.-C. Jiao, W. Liang, and H. Zhang, "A novel low-profile dual circularly polarized dielectric resonator antenna," *IEEE Trans. Antennas Propag.*, vol. 64, no. 9, pp. 4078-4083, Sep. 2016.

[17] P. Jin and R. W. Ziolkowski, "Multi-frequency, linear and circular polarized, metamaterial-inspired, near-field resonant parasitic antennas," *IEEE Trans. Antennas Propag.*, vol. 59, no. 5, pp. 1446-1459, May 2011.

[18] S. A. Saario, J. W. Lu, and D. V. Thiel, "Full-wave analysis of choking characteristics of sleeve balun on coaxial cables," *Electron. Lett.*, vol. 38, no. 7, pp. 304–305, Mar. 2002

[19] T. Shi, M.-C. Tang, Z. Wu, H. Xu, and R. W. Ziolkowski, "Improved signal-to-noise ratio, bandwidth-enhanced electrically small antenna augmented with internal non-Foster elements," *IEEE Trans. Antennas Propag.*, vol.67, no. 4, pp. 2763-2768, Apr. 2019.